Proceedings of the 17th International Heat Transfer Conference, IHTC-17

14 – 18 August 2023, Cape Town, South Africa

IHTC-17 | ID: 125

METHOD FEASIBILITY OF MICRO-CT INVESTIGATION INTO FROST FORMATION

Labuschagne A.*, Zhu T., Bijl H., Rohlfs W.

University of Twente, Drienerlolaan 5, Enschede, 7522NB, Netherlands

ABSTRACT

Air-source heat pumps save energy and reduce emissions but frost formation on the evaporator is still a major challenge. Effective frost mitigation and de-frosting require a fundamental understanding of frost formation dynamics. Previous studies model frost growth and densification within a 15 % error margin, based on bulk and surface properties. However, efficient frost mitigation requires better prediction of local and internal properties including crystal structure. So far, limited optical accessibility has hindered experimental analysis. In this study, a method is proposed to overcome this limitation, through the use of X-ray microcomputed tomography. To test the overall methodological feasibility, additional experimental complexities related to frost melting and instability were mitigated by substituting with a urea-mixture. A sample visually resembling frost was chosen for analysis. A detailed 3-D image of the air/crystal interface, with 7.3 μm spatial resolution, was captured. The porosity of the sample was determined to be 84 %. After filtering, segmenting, and cropping, the image was exported to MATLAB. The effective thermal conductivity and effective mass diffusivity of the sample were determined by solving the respective steady-state three-dimensional diffusion equations. The effective thermal conductivity was determined as 0.0879 W/m.K, which lay between the ideal series and parallel values. The same is true for the effective mass diffusivity of 11.75 mm^2/s. The general methodological feasibility was confirmed by the successful scanning, reconstruction and analysis of the frost substitute.

KEYWORDS: Computed tomography, Experiment, Frost formation, MATLAB, Porosity, Effective thermal conductivity, Effective mass diffusivity, Urea crystals

1 INTRODUCTION

Air-source heat pumps promise significant energy usage and emissions reduction, but frost remains a significant concern. Evaporator frost forms when the evaporator plate surface temperature recedes below the freezing point of water. In air-source heat pumps the system COP is reduced by between 35 % and 60 % [1]. Mitigation strategies and de-frosting/-icing methods require an understanding of the fundamental dynamics of frost formation. The process can be broken into six steps, namely (i)

*Corresponding Author: a.a.labuschagne@utwente.nl

condensate nucleation, (ii) droplet growth and coalescence, (iii) supercooled drop solidification and ice bridging, (iv) crystal growth, (v) frost growth, (vi) frost full growth.

Various authors have already attempted to model the frost growth and densification process but still present some shortcomings. Studies make certain assumptions to address measurement limitations which may affect model accuracy. For instance, Harges and Cremaschi [2, 3] assume all droplets to be uniform, and crystals to be cylinders. Negrelli *et al.* [4] were able to predict the bulk frost layer properties, such as total frost layer thickness or average frost density, of their experiments within a 15 % error margin. Although Leoni *et al.* [5] indicated that application to new datasets tends to result in much poorer performance, highlighting the need to investigate crystal shape.

Addressing the shortcomings through the inclusion of internal and localised properties requires quantification of the internal frost structure. Porosity, mass diffusivity and thermal conductivity should be viewed as a result of this. However, in their review of currently employed measuring techniques, Song and Dang [6] indicate how limited optical accessibility has made real-time experimental identification a severe challenge.

1.1 Novelty

The need exists for new measurement techniques to allow for the quantification of the internal frost crystal structure. In this study, we propose the use of micro-computed tomography (Micro-CT) for application to measurement and subsequent numerical determination of the internal crystal cluster properties.

1.2 Frost and Urea

Frost naturally occurs in cold climate conditions and is only stable while those ambient conditions remain relatively fixed. This presents researchers with much difficulty in their attempts to grow, sample and measure this fragile substance [6, 7]. Micro-CT, in particular, requires mechanically stable (non-melting) samples. To mitigate these risks while investigating the overall methodological feasibility a mixture of urea was selected to act as crystal cluster substitute for this initial study. Urea has the advantage of being stable at room temperature, safe to handle and readily develops into crystal clusters from an aqueous solution, as well as resembling frost on a macroscopic level while also boasting similar x-ray attenuation [8].

2 METHODOLOGY

Grow crystal cluster. The main methodology followed in this study is illustrated in Fig. 1., starting with the growth of a suitable crystal cluster for investigation. The chosen crystal cluster consists of a mixture of urea powder (Sigma Aldrich U5378), PVA (Pattex houtlijm) and dish soap (Dreft). The liquid was prepared by dissolving six tablespoons of urea powder, one teaspoon of PVA and five drops of dish soap in 20 teaspoons of demineralised water at 55 °C.

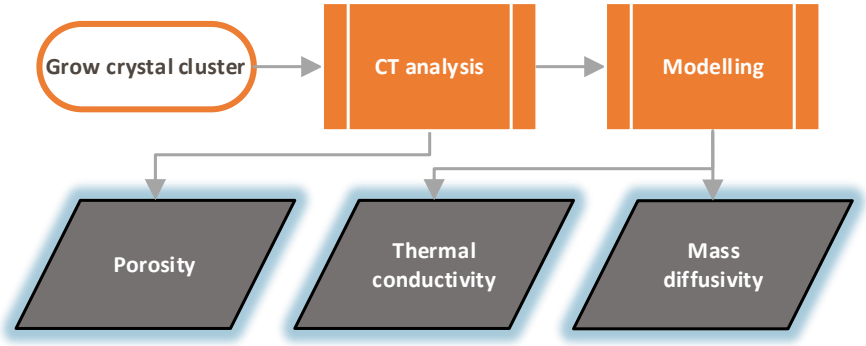

Fig. 1 Main methodological process.

2.1 CT analysis

The next step is CT analysis which is expanded on in Fig. 2. Micro-computed tomography is a measuring technique which allows for non-destructive 3D-imaging of objects down to one micrometre in scale [9]. The process involves taking 2D X-ray images, or radiographs, of an object. The CT scanner used in the current study was the ZEISS Xradia Context.

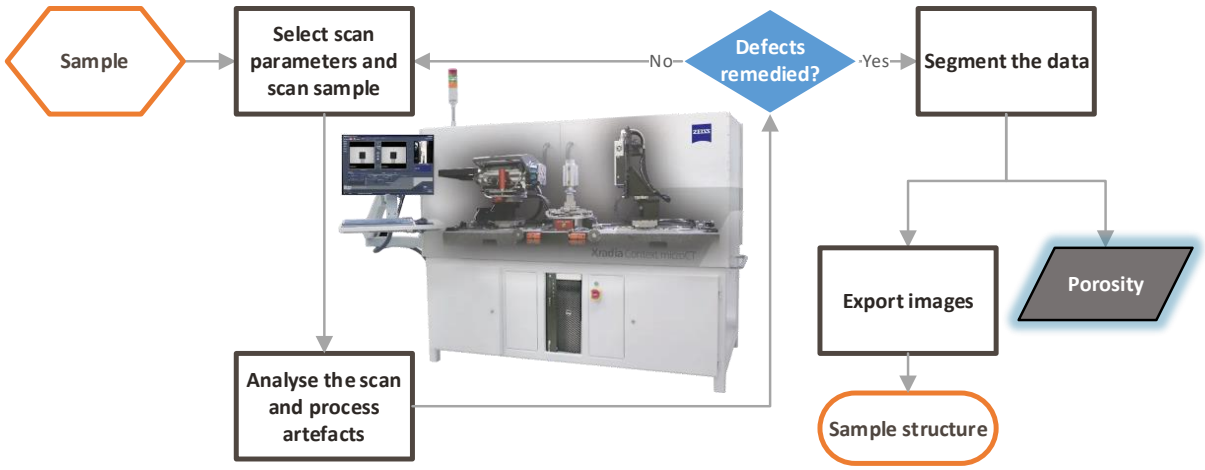

Fig. 2 CT analysis methodology.

Select scan parameters and scan sample. Initial scan parameters are selected based on available literature sources and knowledge of approximate feature sizes. These can be adjusted after each scan to improve the quality of the produced images. The most important parameters are the (a) distance between the sample and x-ray source, (b) distance between the sample and detector, (c) energy settings, (d) number of projections, (e) total exposure time, (f) measurement field, and (g) spatial resolution.

Analyse the scan and process artefacts. After scanning a quality check for flaws, called artefacts, is essential. For X-ray CT scans, the mechanical stability of the sample is of key importance. Blurring is caused when sample motion is greater than the selected voxel length [9]. In 3D scans, a voxel represents the smallest unit which can be used to differentiate between objects/structures. Other artefacts exist, such as streak artefacts when neighbouring materials have too large of a difference in attenuation

coefficients. Some artefacts can be designed for while others, such as noise, are filtered out during post-processing [10, 11]. During this step, the data may also be transferred to new software for post-processing. In this study, the scans were processed via Dragonfly ver. 2022.1 for Windows [12]. Here, the Daubechies 1 wavelet filter was applied for noise removal.

Segment the data. When the data is deemed to be of sufficient quality, segmentation is applied to differentiate between substances. As seen in Fig. 3, voxels with similar attenuations are grouped together and labelled by specifying segmentation limits on a greyscale histogram of the measured voxels [9].

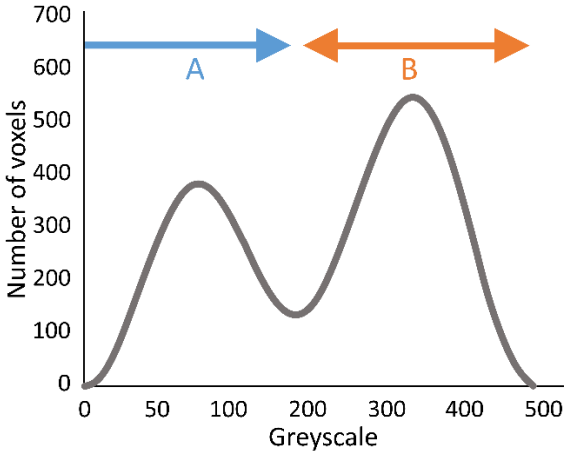

Fig. 3 Micro-CT greyscale segmentation of substances A and B.

Sample noise is removed by using the "process islands" function and the "26-connected" method with a minimum island size of nine voxels. Following this, the largest remaining island is isolated, to represent the main sample. Finally, the data is cropped to reduce the total voxel count which is highly impactful on the MATLAB processing time. Successful segmentation allows for a tally of occupied and empty voxels and thus a determination of porosity.

Export images. The last processing step is to export the processed data, as a stack of 2D black-and-white image files (TIFF).

2.2 Modelling

Fig. 4 shows the basic steps in the MATLAB modelling process. For this study, existing open-source code for solving the steady-state 3D diffusion equation and explicit finite differences scheme was adapted for both temperature and vapour concentration [13]. For simplicity, the two variables were assumed to be uncoupled. When considering a cartesian coordinate system and a non-homogeneous substance, the steady-state diffusion equation may be described as shown in Equation (1).

$$0=\frac{\partial\left(D\frac{\partial\Phi}{\partial x}\right)}{\partial x}+\frac{\partial\left(D\frac{\partial\Phi}{\partial y}\right)}{\partial y}+\frac{\partial\left(D\frac{\partial\Phi}{\partial z}\right)}{\partial z} \quad (1)$$

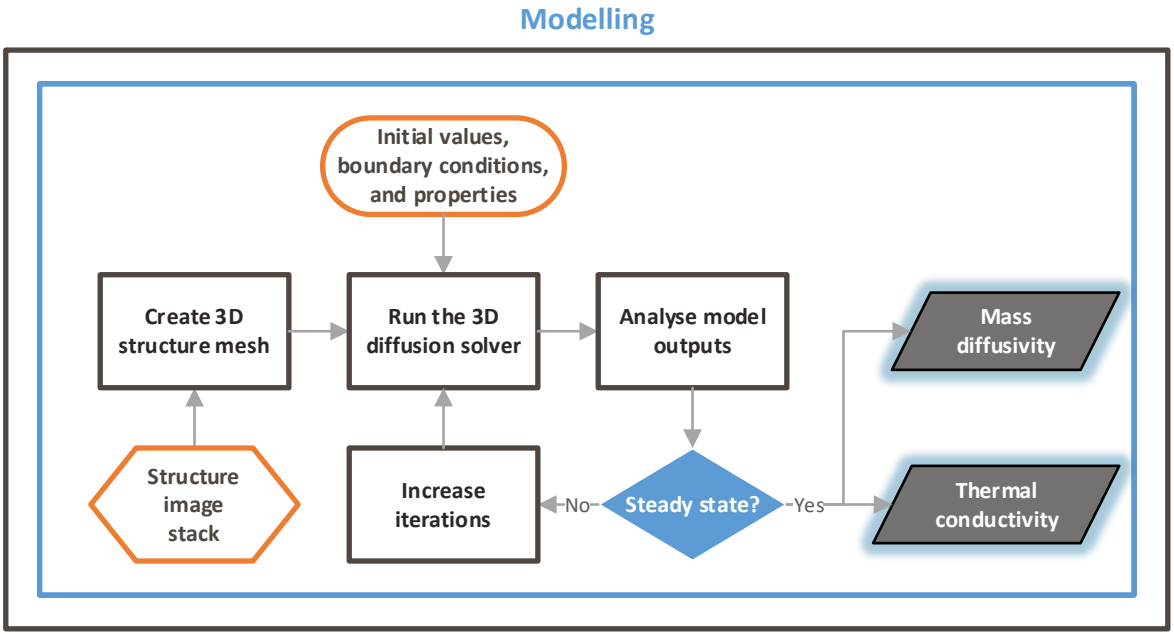

Fig. 4 MATLAB modelling methodology.

Here, Φ represents either the temperature or vapour concentration of an individual volume cell while D is the thermal conductivity or mass diffusivity, respectively and is spatially dependent.

Create 3D structure mesh. The first step is to import each image as 2D matrix using the 'imread' and 'im2double' functions. Doing this effectively creates a 3D matrix wherein each element of the matrix represents either ice (1) or air (0).

Specify model initial values, boundary conditions, and properties. The temperature and vapor concentration in all cells were initially set within a linear range, spanning from the lower boundary condition of -10 °C and 100% relative humidity to the upper boundary condition of 0 °C and 80% relative humidity, both assumed at 1 atm. The sides, front, and back boundaries were insulated, while the material properties remained constant throughout the model, as shown in Table 1.

Table 1 Material properties

Property	Ice	Air
Thermal conductivity (W/m.K)	2.25	0.0244
Mass diffusivity (mm^2/s)	0.025	21.9
Density (kg/m^3)	917	1.29

Analyse model outputs. A check is made that the model is stable and that outputs have converged. If satisfied, the mass diffusivity and thermal conductivity are calculated. Both are compared to their respective idealised values for series and parallel resistances, as shown in Equation (2) and (3).

$$D_{series} = \left(\frac{\alpha_{ice}}{D_{ice}} + \frac{(1-\alpha_{ice})}{D_{Air}}\right)^{-1} \quad (2)$$

$$D_{\text{parallel}} = D_{\text{ice}} \cdot \alpha_{\text{ice}} + D_{\text{air}} \cdot (1 - \alpha_{ice}) \quad (3)$$

D_{series} and D_{parallel} refer to the ideal 2-layer/column series and parallel calculation of the thermal conductivity or mass diffusivity. D_{air} and D_{ice} are the case-specific values for air and ice, as found in Table 1 while α_{ice} is the sample's overall volumetric ice fraction.

3 RESULTS & DISCUSSION

3.1 Sample crystals

Crystal growth on all samples presented as a needle-type structure, with flat samples producing a crystal layer bed before branching. The flat PVA-laminated filter paper sample, as seen in Fig. 5, was identified as the most promising specimen and subsequently selected for further study. The sample thickness varied between 0.6 mm and 3.0 (+-0.1) mm which is very similar to a frost layer grown over two hours [5]. The sample size was approx. 12.2 mm x 12.5 mm.

Fig. 5 Urea-mixture sample most resembling frost, grown on flat PVA-laminated filter paper.

3.2 CT analysis

Table 2 shows the parameters used in two scans of the sample. Although the first scan showed sufficient resolution and general clarity it was not appropriate for segmentation due to the presence of streak artefacts reaching as high as 0.8 mm from the mounting surface, see Fig. 6. This was resolved in the second scan through the addition of double-sided foam tape between the mounting and sample.

Table 2 CT scan parameters

Parameter	Scan 1	Scan 2
Distance to source (mm)	23.59	27.24
Distance to detector (mm)	474.01	530.95
Voltage (kV)	90	60
Amperage (µA)	88.63	82.74
Number of projections	4501	9501
Total exposure time (hh:mm:ss)	03:45:03	07:55:03
Measurement field (l·w·h mm^3)	10.72·10.78·6.85	11.02·11.18·7.03
Spatial resolution (µm/pixel)	7.09	7.30

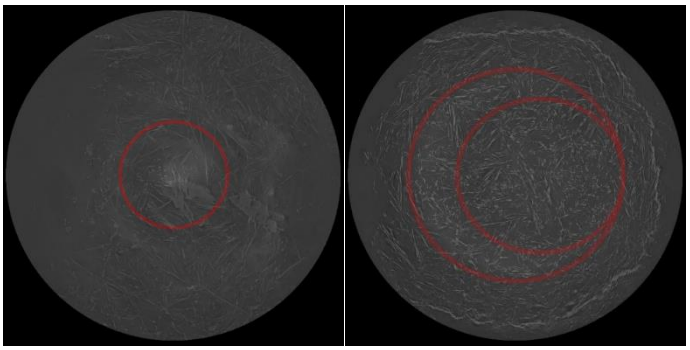

(a) (b)

Fig. 6 Streak artefact progressing from (a) inside the red circle, at the sample centre to (b) between the red circles, closer to the sample extremities with increasing distance from the mounting.

After segmentation, the final porosity was determined as 84.43 %. The final TIFF image stack consisted of 200 images of 100 by 100 pixels in black (air) and white (crystal) with varying crystal density, as seen in Fig. 7.

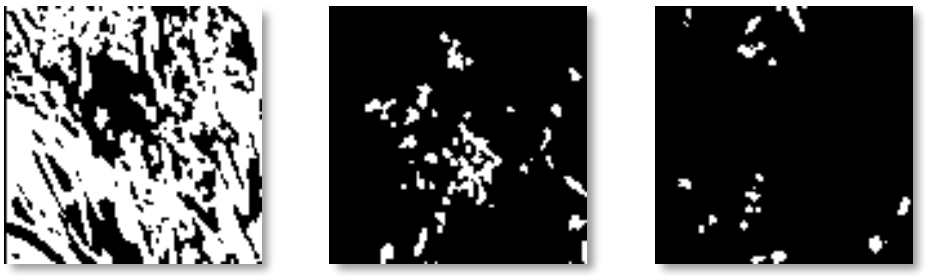

(a) (b) (c)

Fig. 7 Exported image of sample voxel (a) layer 1, (b) layer 100, and (c) layer 200, where white pixels represent ice and black pixels represent air.

3.3 Modelling

The model ran for 23 444 iterations before both temperature and vapour concentration had converged to the 8th significant figure. The calculated effective thermal conductivity of 0.0879 W/m.K is showcased in Fig. 8 along with the sample average density of 143.9 kg/m^3. The idealised series and parallel configuration thermal conductivities are also shown as 0.0288 W/m.K and 0.371 W/m.K respectively which indeed bound the effective thermal conductivity as expected.

Fig. 9 shows the effective mass diffusivity of 11.75 mm^2/s along with the ideal series and parallel configuration diffusivities of 0.1596 mm^2/s and 18.49 mm^2/s. Once again these values bound the effective diffusivity as expected.

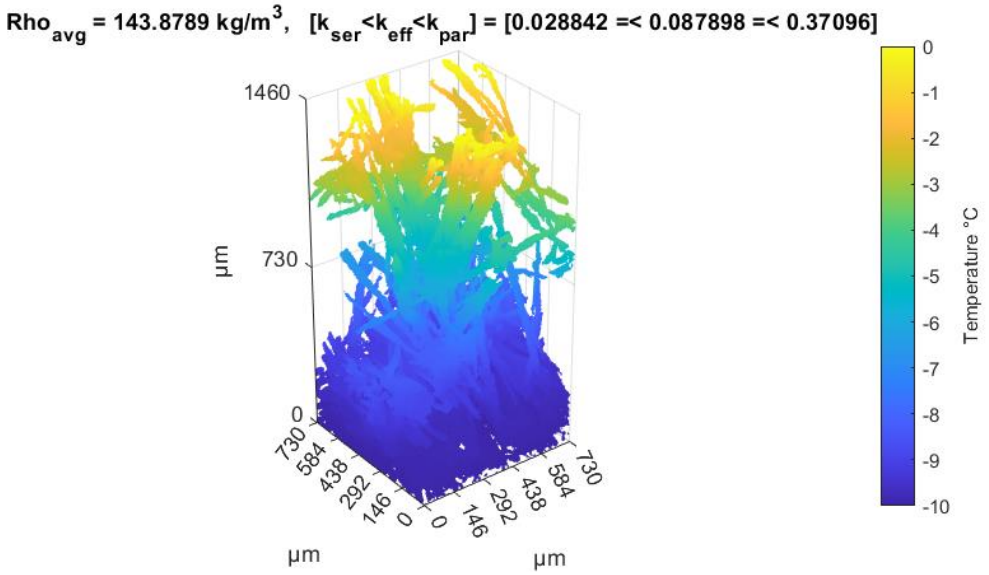

Fig. 8 Surface plot of the crystal structure displaying the temperature gradient, average density and thermal conductivity compared to ideal values.

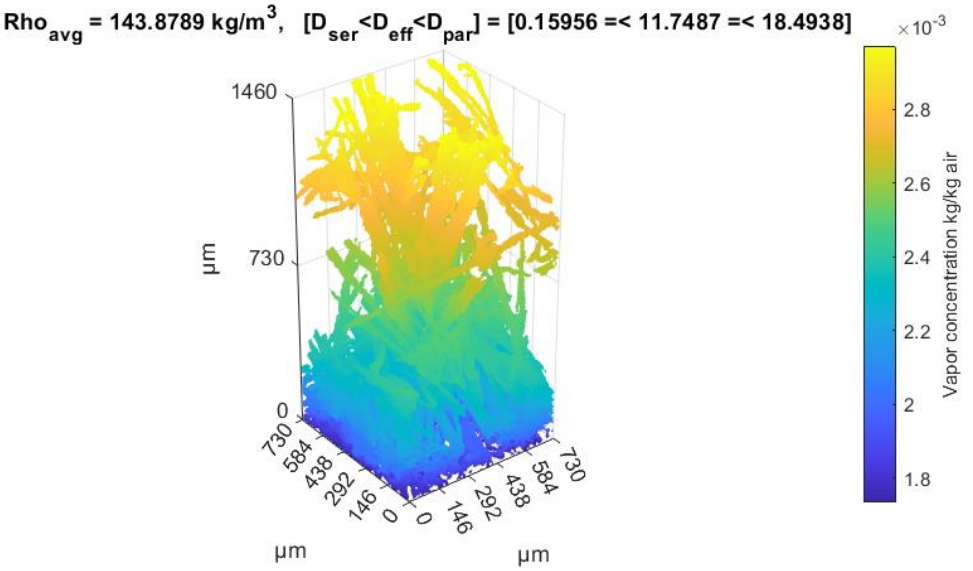

Fig. 9 Surface plot of the crystal structure displaying the concentration gradient, average density and mass diffusivity compared to ideal values.

Fig. 10 shows the average density and effective thermal conductivity of each layer as solid lines. The layer-averaged thermal conductivity is also represented by the dashed line. In the left-most section of the graph, the thermal conductivities both follow the trend of the density profile. They deviate from this soon after when the crystals tend to rotate away from a horizontal to a vertical orientation, maintaining a higher relative thermal conductivity in the upper section of the sample. The effective thermal conductivity is also shown to differ from the layer-averaged thermal conductivity due to the formation of non-contributing zones in the complex crystal structure, see the work of Seppälä [14] for elucidation.

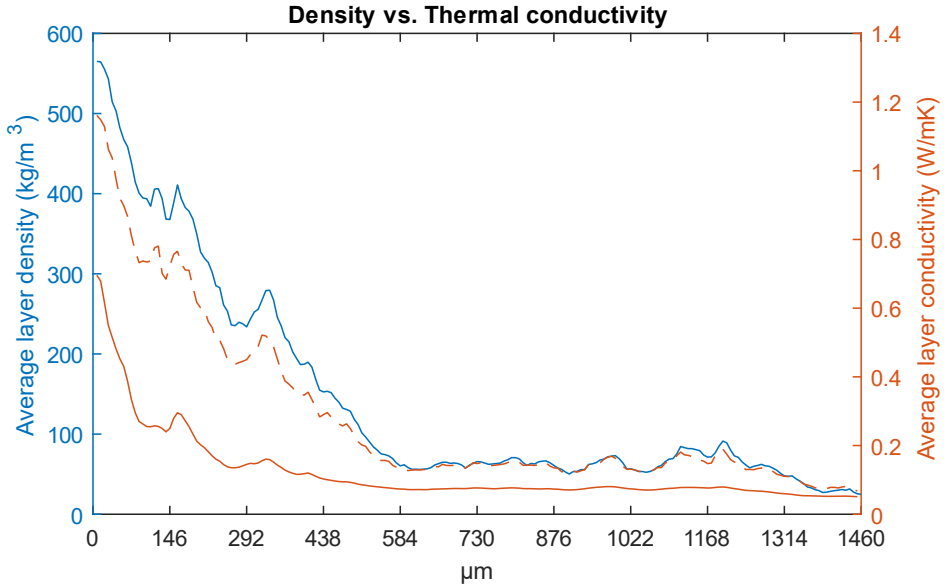

Fig. 10 Average density, effective thermal conductivity and layer-averaged thermal conductivity over the sample height.

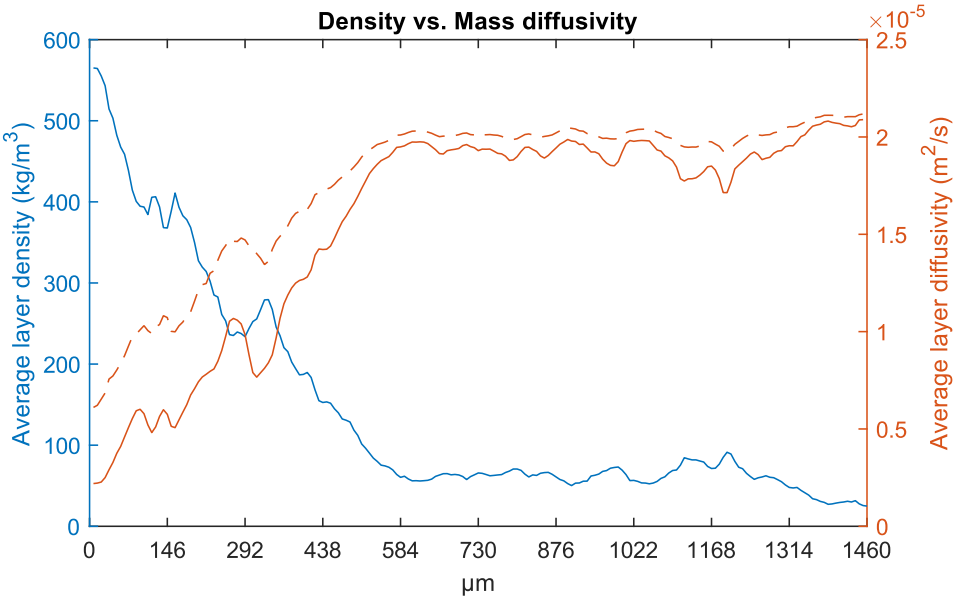

Fig. 11 Average density, effective mass diffusivity and layer-averaged mass diffusivity over the sample height.

Fig. 11 shows similar information as Fig. 10, but for the mass diffusivity. Average density and effective thermal conductivity of each layer are shown as solid lines. The effective mass diffusivity differs from the layer-averaged diffusivity for the same reason as the thermal conductivities, namely the formation of non-contributing zones in the complex crystal structure and highlights the importance of knowing the crystal shape when estimating effective mass diffusivity and thermal conductivity values.

4 CONCLUSION

A sample resembling frost was successfully grown on flat laminated filter paper. The sample could be scanned in a CT-scanner and the data processed. A cropped-sample porosity of 84.43 % was determined and the sample structure was exported to MATLAB. The 3D diffusion equation was successfully run and converged after 23 444 iterations. The final sample density was determined as 143.9 kg/m^3 with an effective thermal conductivity of 0.0879 W/m.K and an effective mass diffusivity of 11.75 m^2/s, both of which were bounded by the ideal values and varied throughout the height of the sample, depending on the crystal shape. Finally, the effect of non-contributing zones on the deviation from layer-averaged conductivity of diffusivity values was identified. With this, the general methodological feasibility is confirmed and the process can be further adapted for real frost.

NOMENCLATURE

x,y,z	Cartesian spatial dimension	[-]
Φ	Temperature/Vapour concentration	[°C | -]
D	Thermal conductivity/mass diffusivity	[W/m.K | mm^2/s]
α_{Ice}	Volumetric ice fraction	[-]

REFERENCES

[1] Y. Li, M. Li, Y. Utaka, T. Daitoku, H. Ohkubo, and C. Yang, "Scraping force characteristics of frost formed on vertical cooling surfaces having different structures and wettability," *Int. J. Refrig.*, 101, pp. 148–154, (2019). **Journal Paper**

[2] E. Harges, *Experimental and Analytical Investigation of Early Frost Growth on Surfaces with Varying Wettability under Typical Heat Pump Operating Conditions*, Ph.D. Thesis, Auburn University, (2021). **Dissertation**

[3] E. Harges and L. Cremaschi, "Effects of crystal formation on the initial frost thickness and density on cold surfaces," *Int. J. Refrig.*, 136, pp. 82–93, (2022). **Journal Paper**

[4] S. Negrelli, R. P. Cardoso, and C. J. L. Hermes, "A finite-volume diffusion-limited aggregation model for predicting the effective thermal conductivity of frost," *Int. J. Heat Mass Transf.*, 101, pp. 1263–1272, (2016). **Journal Paper**

[5] A. Leoni, M. Mondot, F. Durier, R. Revellin, and P. Haberschill, "Frost formation and development on flat plate: Experimental investigation and comparison to predictive methods," *Exp. Therm. Fluid Sci.*, 88, pp. 220–233, (2017). **Journal Paper**

[6] M. Song and C. Dang, "Review on the measurement and calculation of frost characteristics," *Int. J. Heat Mass Transf.*, 124, pp. 586–614, (2018). **Journal Paper**

[7] R. Matsumoto, T. Uechi, and Y. Nagasawa, "Three-dimensional microstructure of frost layer measured by using X-ray μCT," *J. Therm. Sci. Technol.*, 13(1), pp. JTST0014, (2018). **Journal Paper**

[8] P. Li, G. He, D. Lu, X. Xu, S. Chen, and X. Jiang, "Crystal size distribution and aspect ratio control for rodlike urea crystal via two-dimensional growth evaluation," *Ind. Eng. Chem. Res.*, 56(9), pp. 2573–2581, (2017). **Journal Paper**

[9] P. J. Withers *et al.*, "X-ray computed tomography," *Nat. Rev. Methods Primers*, 1(1), pp. 1–21, (2021). **Journal Paper**

[10] S. D. Rawson, J. Maksimcuka, P. J. Withers, and S. H. Cartmell, "X-ray computed tomography in life sciences," *BMC Biol.*, 18(1), pp. 1–15, (2020). **Journal Paper**

[11] B. R. Pinzer, A. Medebach, H. J. Limbach, C. Dubois, M. Stampanoni, and M. Schneebeli, "3D-characterization of three-phase systems using X-ray tomography: tracking the microstructural evolution in ice cream," *Soft Matter*, 8(17), pp. 4584–4594, (2012). **Journal Paper**

[12] Object Research Systems (ORS) Inc, "Dragonfly 2022.1." Retrieved Dec. 15, 2022, from https://theobjects.com/dragonfly/index.html, (2022). **Computer Program**

[13] A. Pedcenko, "3D Heat equation solution with FD in MATLAB." Retrieved Dec. 18, 2022, from https://github.com/aa3025/heat3d/releases/tag/1.0.5, (2022). **Computer Program**

[14] A. Seppälä, "Efficient method for predicting the effective thermal conductivity of various types of two-component heterogeneous materials," *Int. J. Therm. Sci.*, 134, pp. 282–297, (2018). **Journal Paper**